Supporting information for:

Design, synthesis and characterization of hierarchical porous stacked thin films based on MOFs and ordered mesoporous oxides

Melina Arcidiácono[1], Juan A. Allegretto[1,2], Omar Azzaroni[1], Paula C. Angelomé[3], Matías Rafti[1]

(1) Instituto de Investigaciones Fisicoquímicas Teóricas y Aplicadas (INIFTA), Departamento de Química, Facultad de Ciencias Exactas, Universidad Nacional de La Plata, CONICET, CC 16 Suc. 4, B1904DPI, La Plata, Argentina
(2) Laboratory for Life Sciences and Technology (LiST), Department of Medicine, Faculty of Medicine and Dentistry, Danube Private University,3500 Krems, Austria.
(3) Gerencia Química & INN, Centro Atómico Constituyentes, Comisión Nacional de Energía Atómica, CONICET, Av. General Paz 1499, 1650, San Martín, Buenos Aires, Argentina

1. Procedures for the synthesis of ZIF-8 nanoparticles employed for spin coating (SC)

Films prepared via deposition using nanoparticles with spin coating are highly dependent on the shape, size and dispersibility of the colloidal units employed. In this study, we aim to obtain uniformly distributed MOF layers with low roughness and controlled thickness. Achieving a homogeneous dispersion of nanoparticles without agglomeration is thus crucial. It is well-known that drying and redispersing nanoparticles is challenging because it leads to the formation of some degree of agglomeration. Having in mind that such an approach might be useful for the standardization of procedures using dried powders to prepare on-demand colloids, we studied the influence of different purification procedures on the colloidal suspensions. Namely, we compared as-prepared ZIF-8 colloids, and ZIF-8 colloids obtained from redispersion of dried powders.

As mentioned in the main text, ZIF-8 synthesis with a (1:4) molar ratio of (metal:linker) was carried in methanol and then, fresh solvent exchange purification steps for the removal of unreacted MOF precursors were applied. The resulting purified colloidal suspensions were subjected to different procedures, namely, **I) (re-dispersed)** drying, followed by redispersion in the same amount of methanol under stirring (4 hour) and low G centrifugation steps to precipitate aggregates and large particles (less than 1200 RPM or 300 G), **II) (as-prepared)** low G centrifugation and direct use. The colloids obtained with different centrifugation conditions were examined using dynamic light

scattering (DLS) for both processes (see correlation curves for both procedures in **Figure S1 A)** and **B)**). It can be clearly observed that re-dispersion yields non-stable colloids, unless low G centrifugation steps are followed, while as-prepared colloids remain quite stable regardless of the procedure followed. Having in mind that spin coating requires colloidal stability for a homogeneously distributed film, as-prepared suspensions subjected to 1200 rpm centrifugation were chosen. DLS intensity size distribution obtained is centred in approximately 70 nm as shown in **Figure S1 D)**, for the sake of completeness, a typical SEM image corresponding to the products obtained for the molar ratio employed is shown in **Figure S1 C)** (monodisperse 40-60 nm particles), and Nitrogen adsorption from which a BET surface area of 1564 m^2/g can be estimated is presented in **Figure S1 E).**

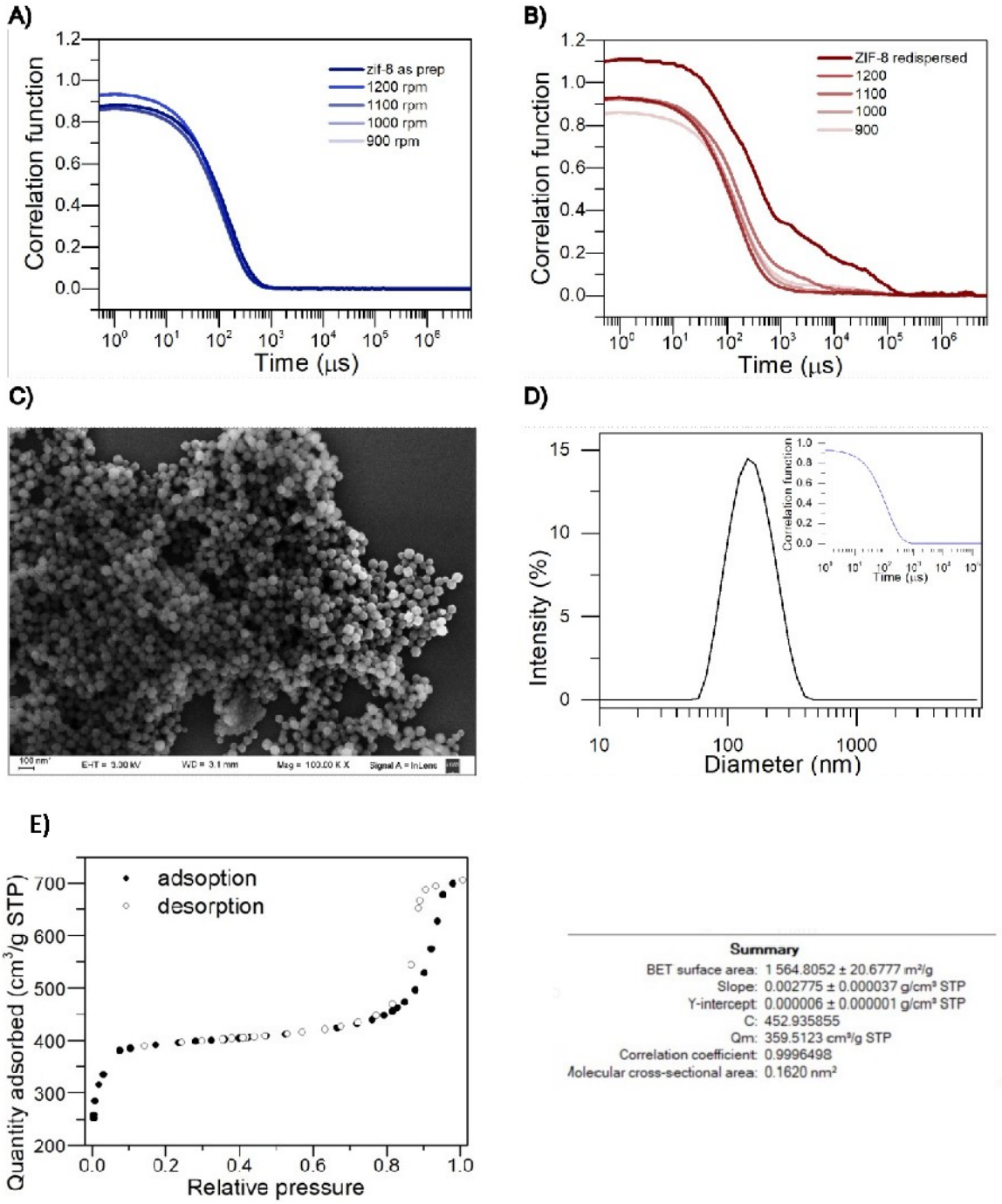

FIGURE S1. Characterization of colloidal suspensions of ZIF-8 nanoparticles obtained employing different procedures as detailed above. **A)** as-prepared ZIF-8 nanoparticles DLS correlation function for different centrifugation velocities. **B)** redispersed ZIF-8 nanoparticles DLS correlation function for different centrifugation velocities. **C)** SEM image of the as-prepared ZIF-8 nanoparticles. **D)** Intensity DLS size distribution. **E)** Nitrogen adsorption isotherm showing microporosity accessible and a mild hysteresis loop for high relative pressures. BET area calculation results.

2. **Characterization with Spectroscopic Ellipsometry of 5x-ZIF-8-LPE.** The optical model fit (a Cauchy layer) employed for SE experiments carried on 5x-ZIF-8 LPE films is shown below in **Figure S2**.

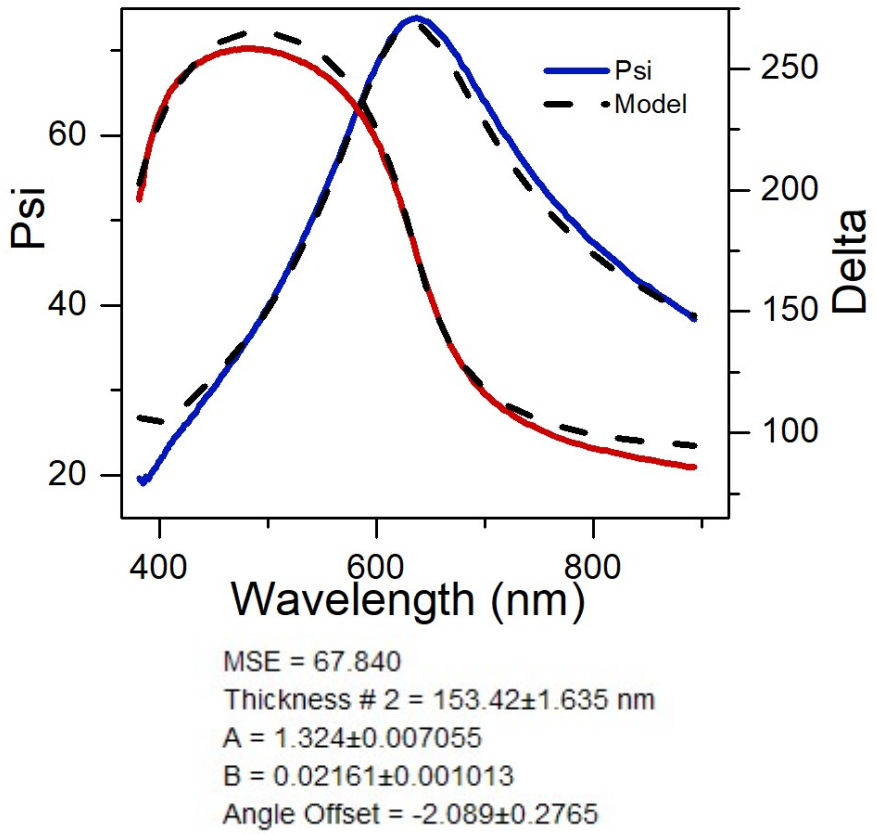

FIGURE S2. Ellipsometry experiments and model fit parameters for 5x-ZIF-8-LPE film.

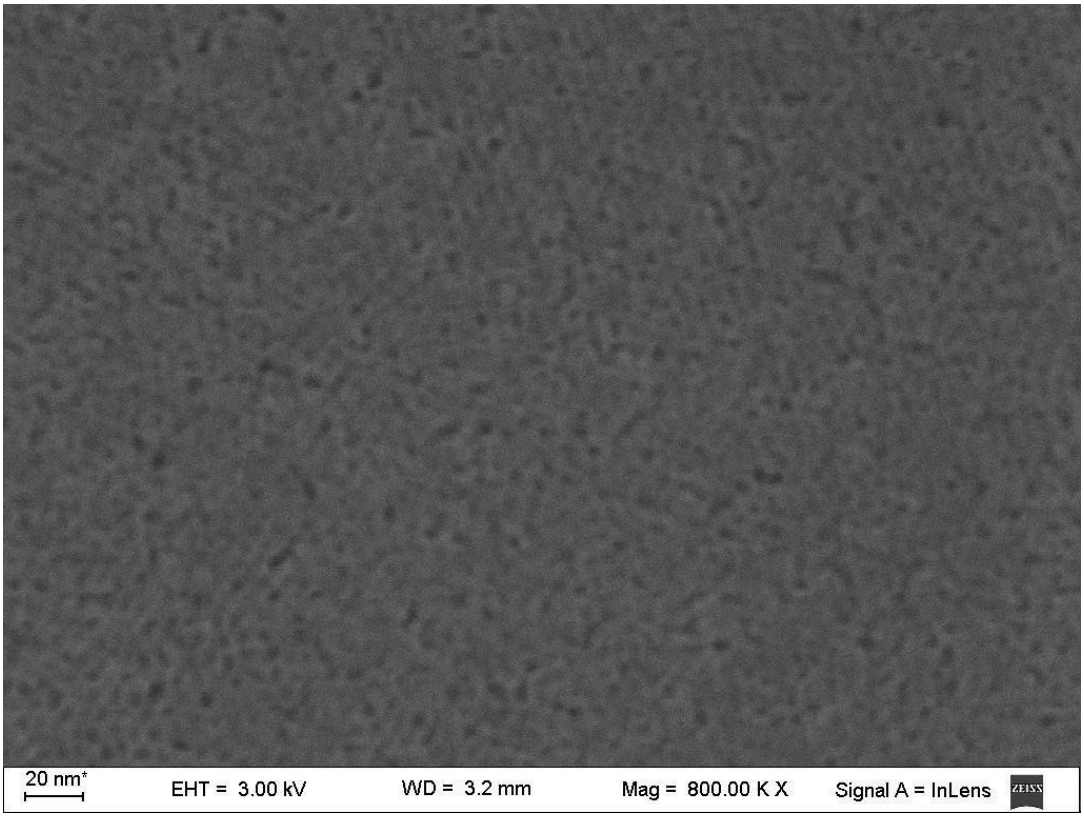

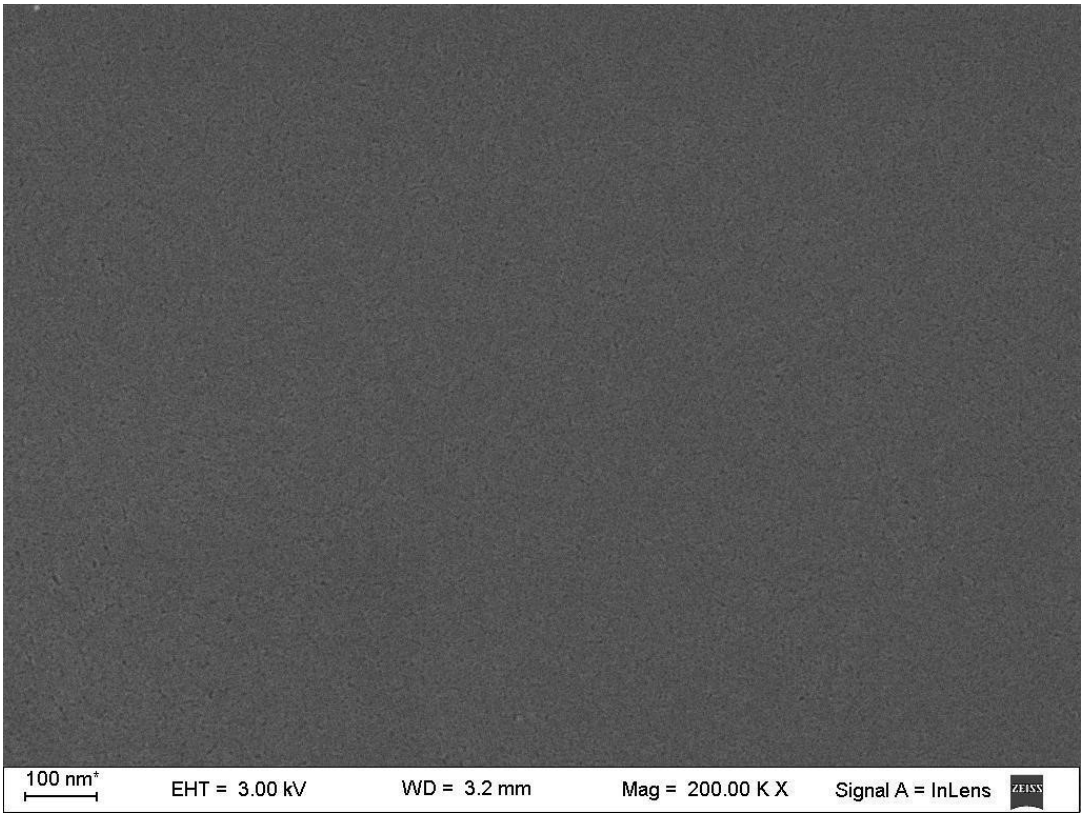

FIGURE S3. SEM for TB mesoporous layer, at different magnifications.

3. Characterization of TF and SB mesoporous layers

TF 200+EE and SB 200+EE films were characterized with XRR, measuring at high (90-91%) and low (7-8%) relative humidity. The displacement of the critical angle position shows the accessibility of pores. The Kiessig fringes demonstrate the homogeneity on the films thicknesses.

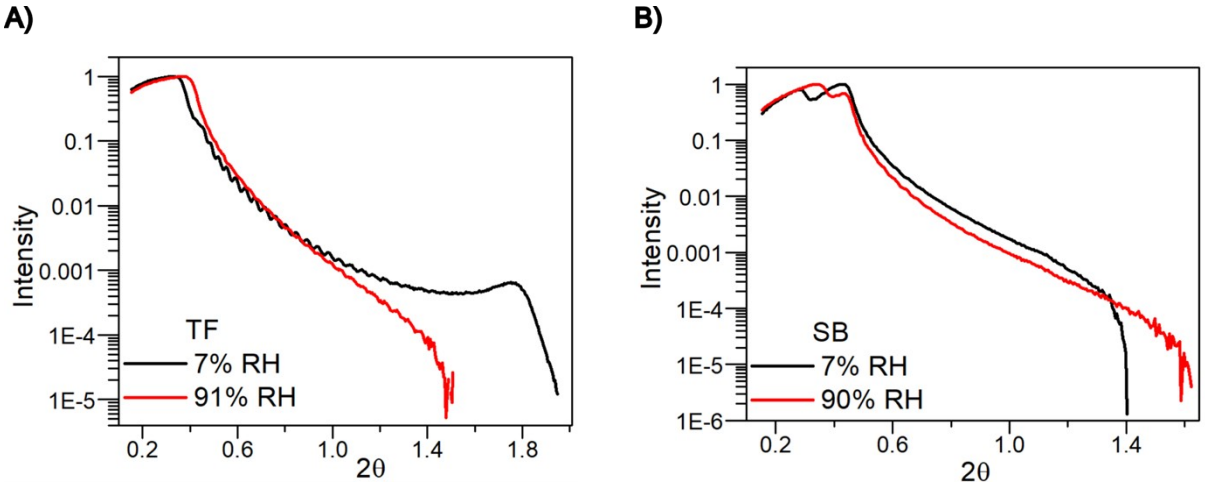

FIGURE S4. XRR experiments for A) TF 200+EE and B) SB 200+EE mesoporous layers.

4. Characterization of TB 350 mesoporous layers

Mesoporous TB 350 sample was characterized using XRR under dry and vapor saturated atmospheres. Pore accessibility and homogeneity stability of the film are demonstrated by the shift in critical angle and the Kiessig fringes observed.

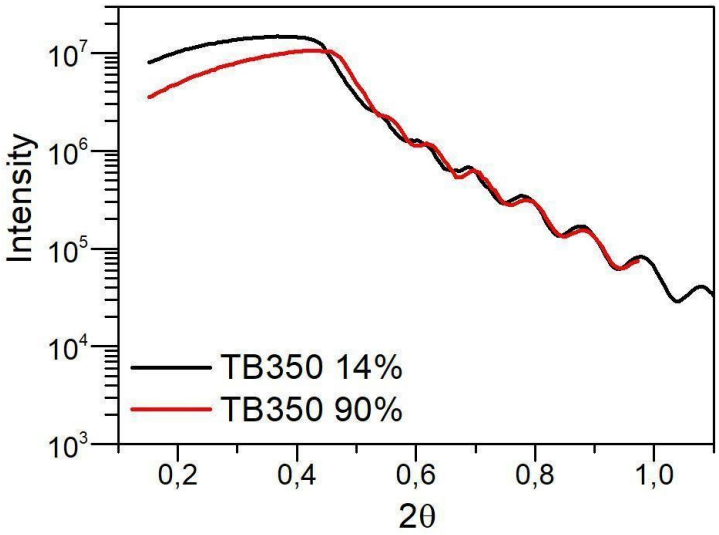

FIGURE S5. XRR experiments for TB 350 mesoporous layer.

5. Characterization with Spectroscopic Ellipsometry of ZIF-8-SC.

Alternative exposure to N2 and H2O were carried and SE measurements were employed for evaluating the accessibility of the porosity present. As can be seen in Figure S7, no changes were observed in Delta and Psi after 2 hours exposure to water vapor saturated flow. This is the reason why XRR experiments for the evaluation of pore accessibility yield no usable results.

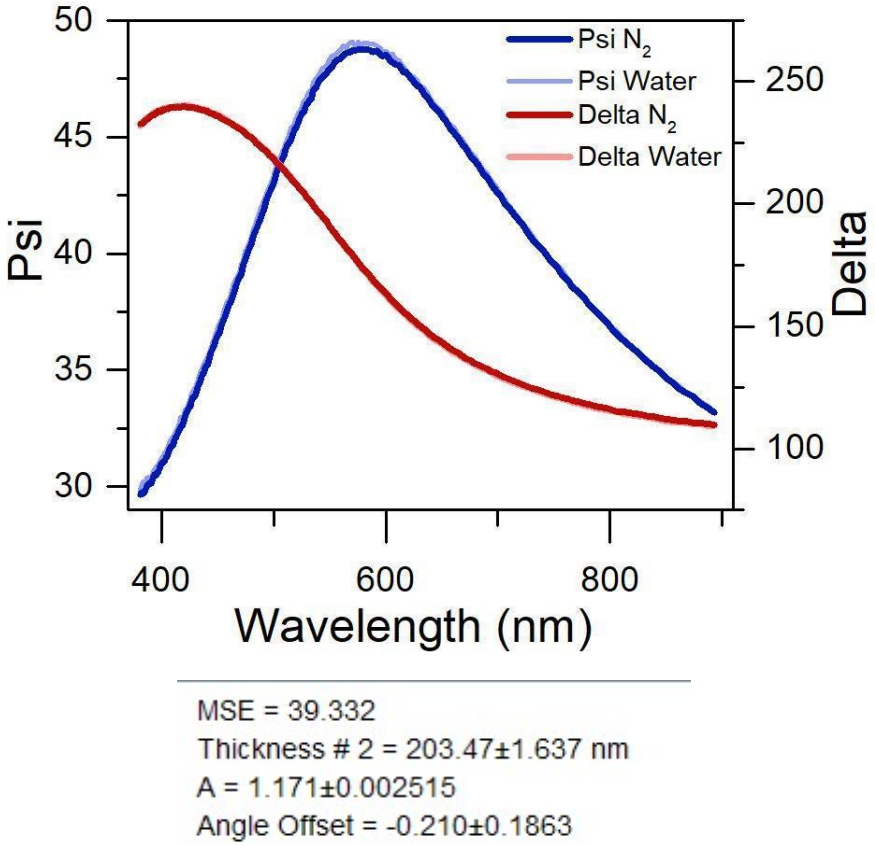

FIGURE S6. Ellipsometry experiments and model fit parameters for ZIF-8-SC film exposed to dry and vapor saturated flow.

6. XRR measurements for bilayers showing full range.

XRR experiments presented in main text Figure 3 are limited to a short 2θ range in order to highlight the critical angle shift of prepared bilayers. Here, for completeness, full range XRR experiments are shown and Kiessig fringes are observable in all cases for bilayers.

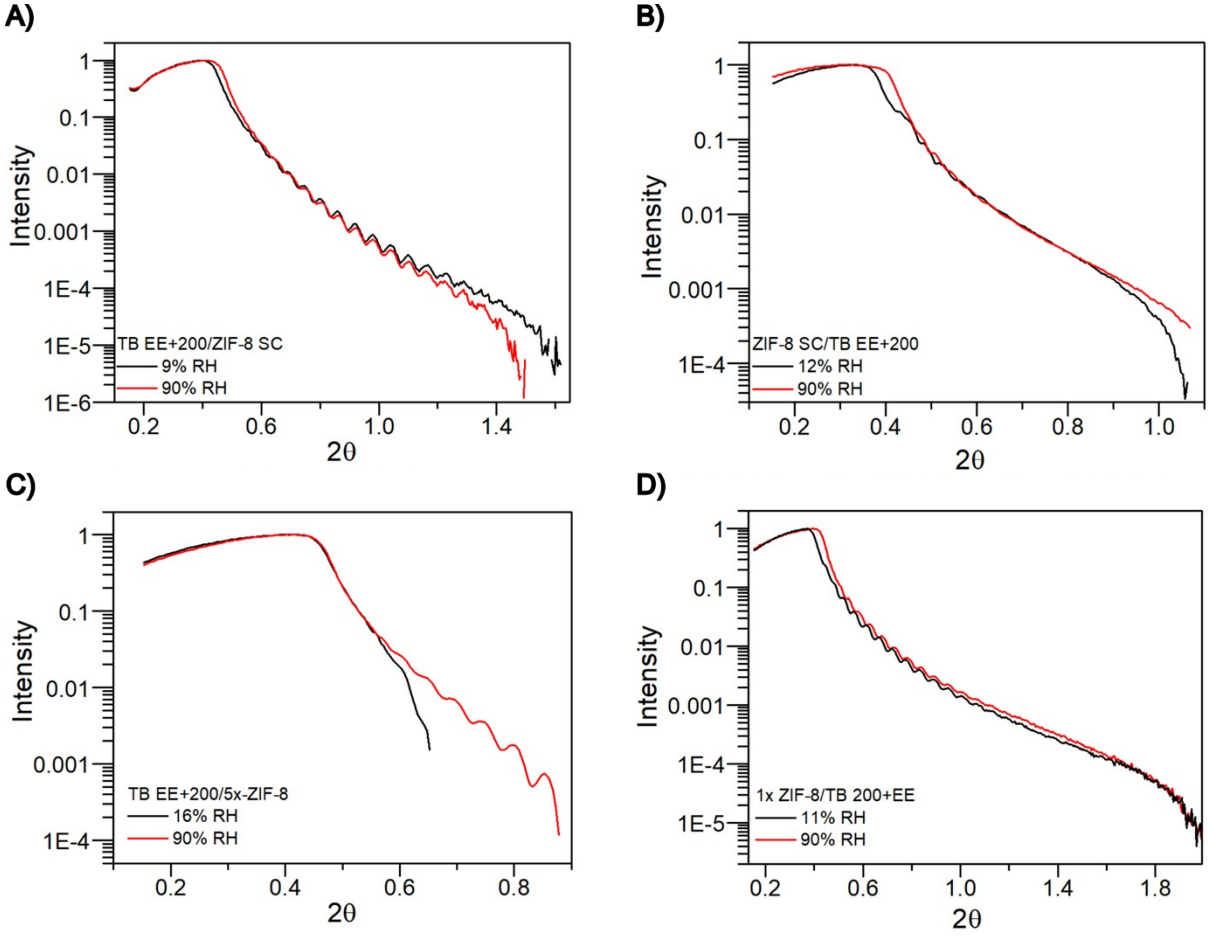

FIGURE S7. XRR experiments carried out for different bilayers (indicated in the labels) displaying full range in 2θ.

7. GI-XRD for 1x-ZIF-8 LPE/TB 200+EE

The experiments carried for 1x-ZIF-8 LPE/TB 200+EE show the typical low angle peak corresponding to meso-organization of the TB layer.

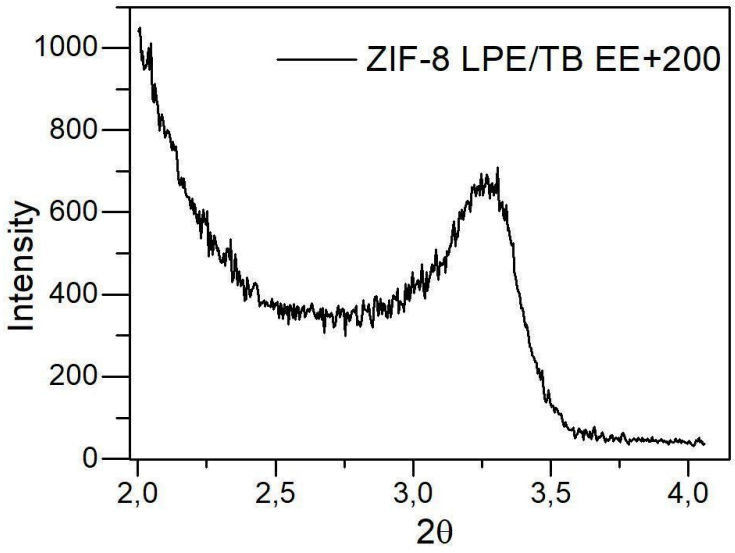

FIGURE S8. GI-XRD experiments showing the low angle peak arising from pore ordering in the TB mesoporous layer.

8. Original SEM and TEM images

For the sake of completeness, SEM and TEM images presented in the main text are reproduced here for the full image range in order to illustrate the homogeneity of the morphologies and sizes observed.

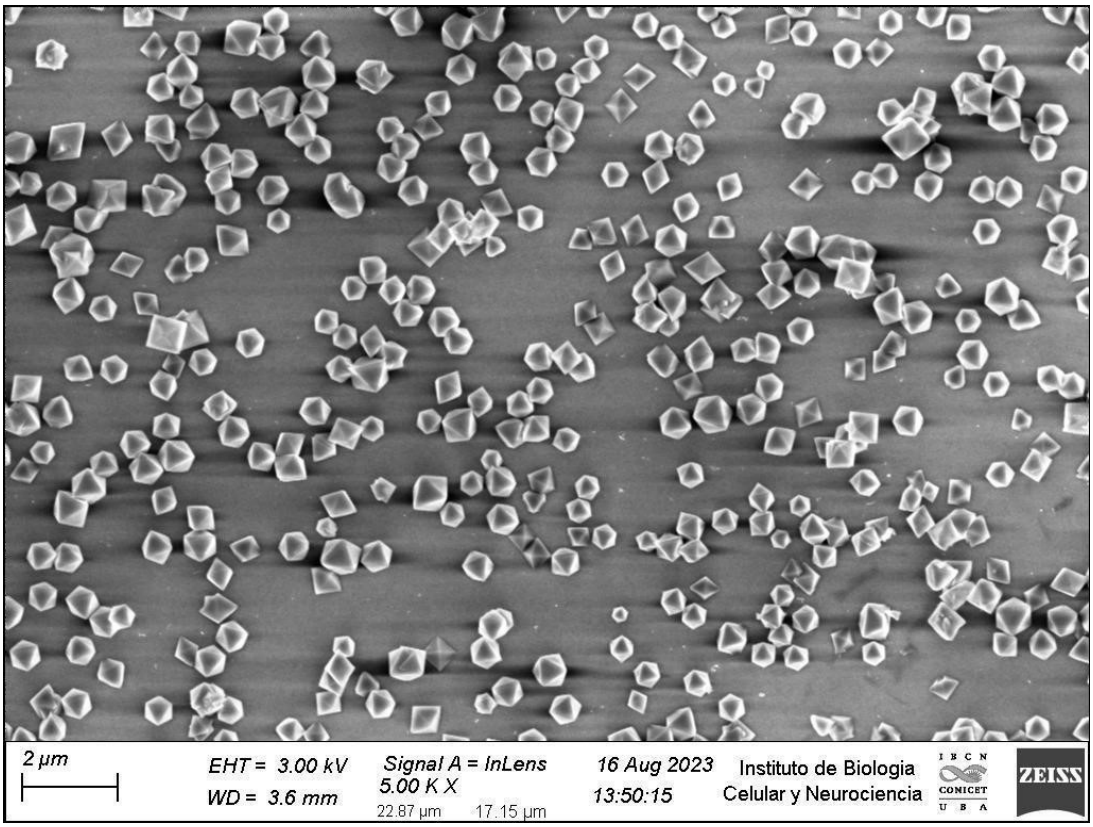

FIGURE S9. SEM for TB 350/UiO-66 sample

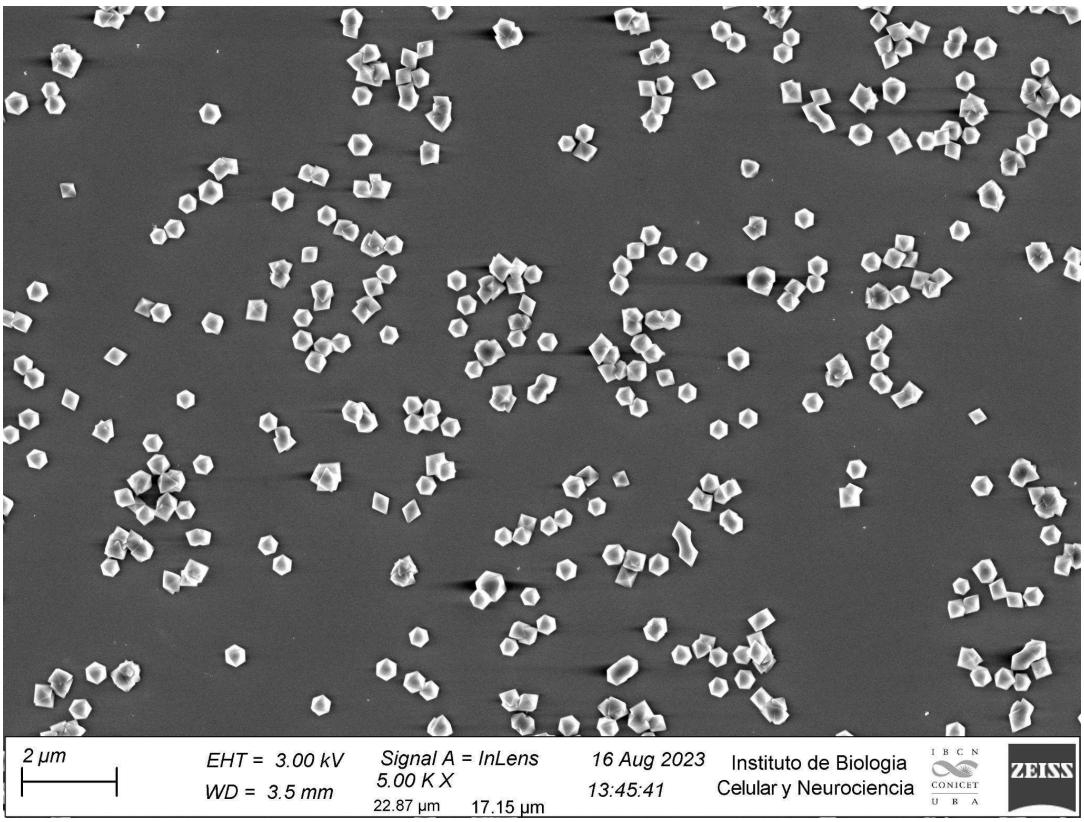

FIGURE S10. SEM for TB EE+200/UiO-66 sample

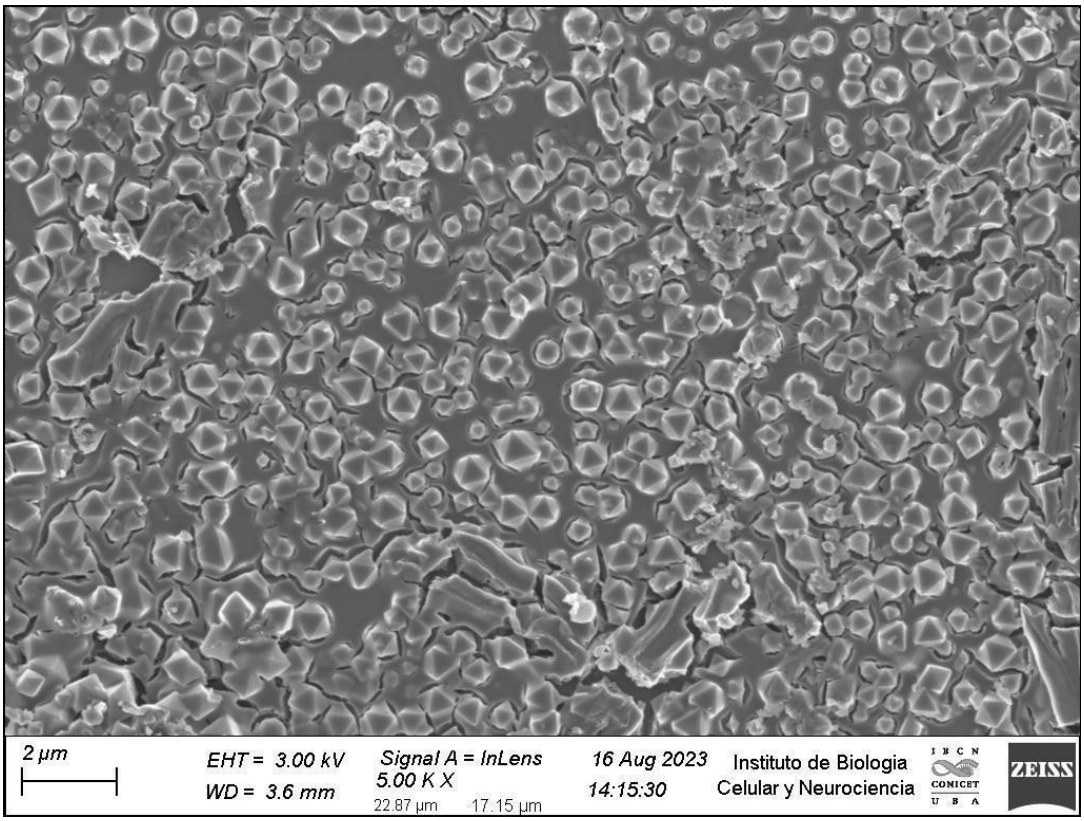

FIGURE S11. SEM for UiO-66/TB 200+EE sample

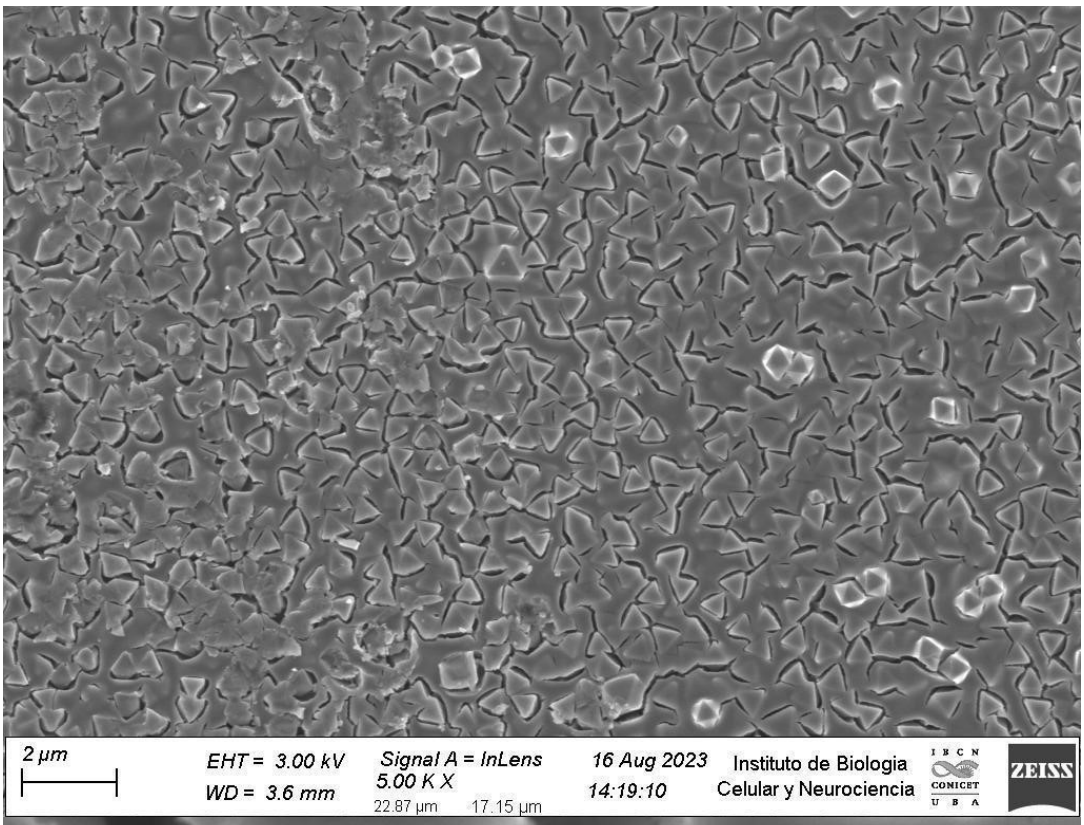
2 µm
EHT = 3.00 kV
WD = 3.6 mm
Signal A = InLens
5.00 K X
22.87 µm 17.15 µm
16 Aug 2023
14:19:10
Instituto de Biologia
Celular y Neurociencia
I N C N
CONICET
U B A
ZEISS

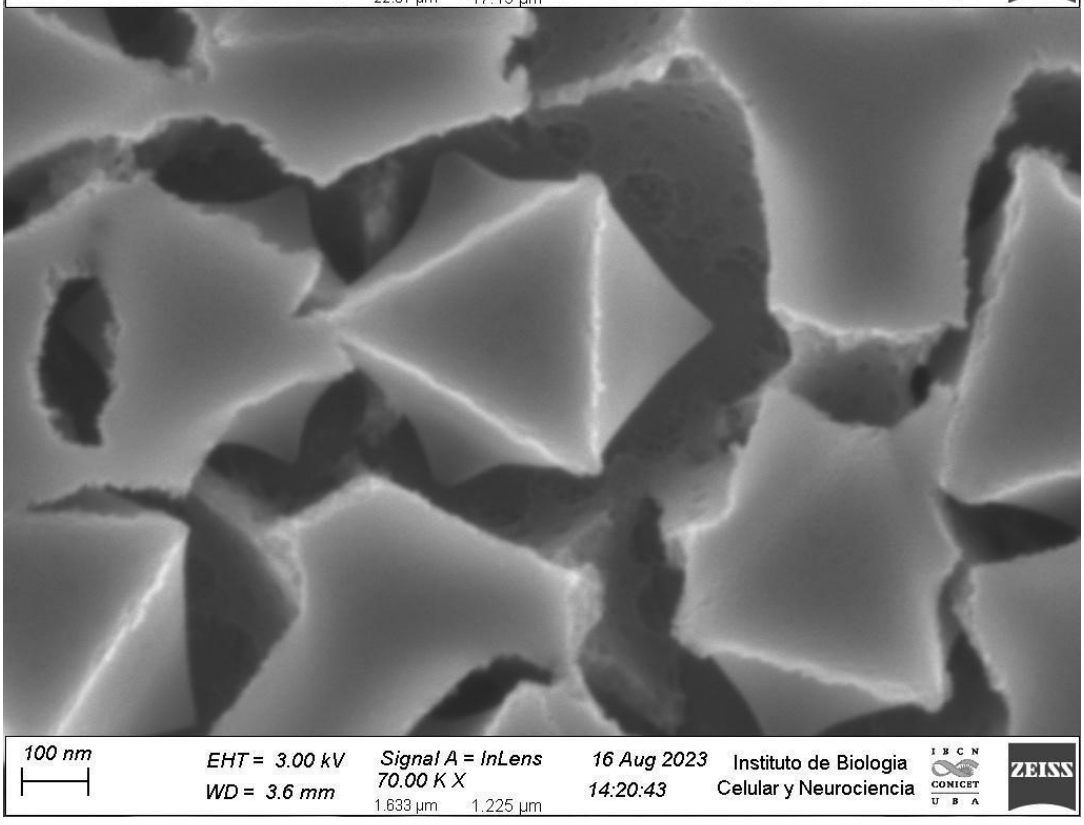
100 nm
EHT = 3.00 kV
WD = 3.6 mm
Signal A = InLens
70.00 K X
1.633 µm 1.225 µm
16 Aug 2023
14:20:43
Instituto de Biologia
Celular y Neurociencia
I N C N
CONICET
U B A
ZEISS

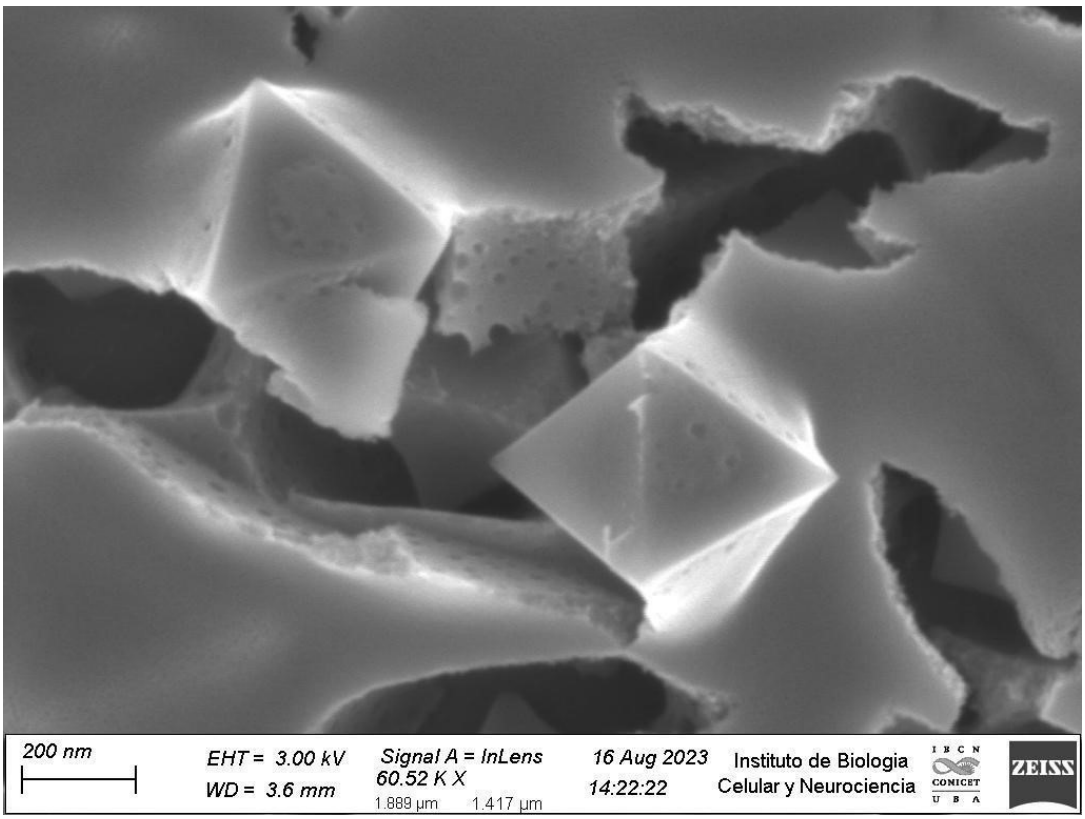

FIGURE S12. SEM of UiO-66/TF 200+EE sample, at different magnifications

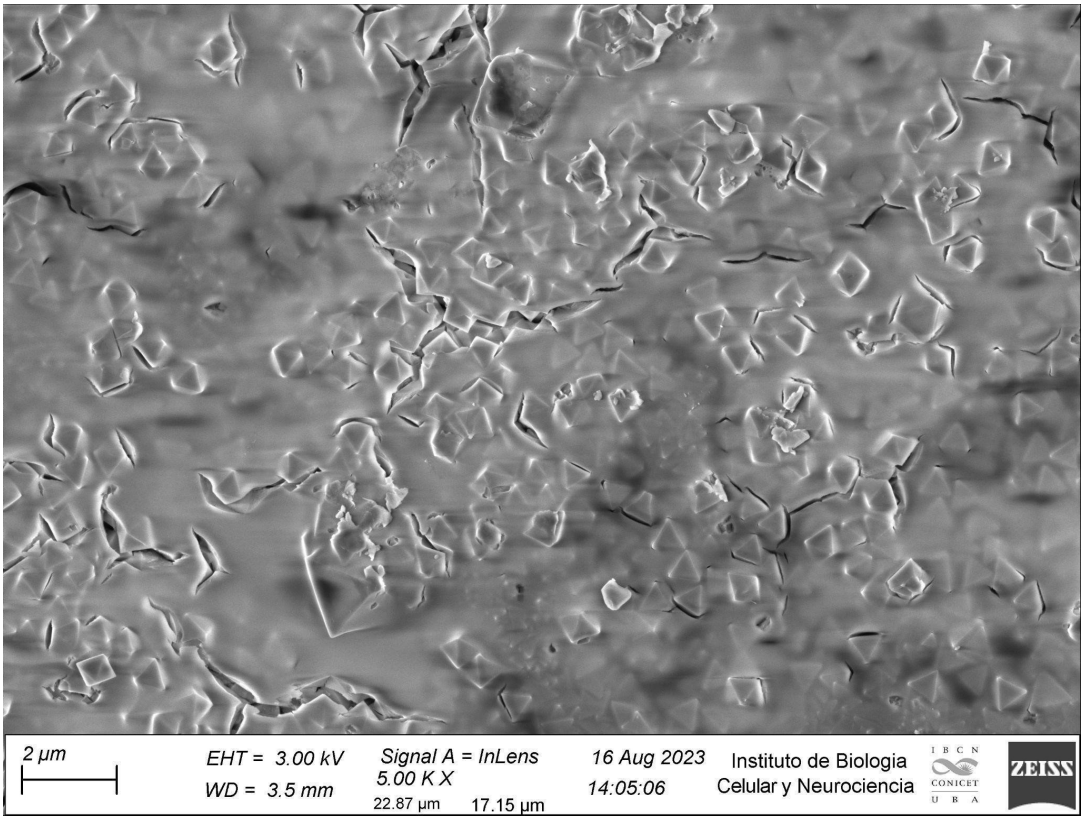

FIGURE S13. SEM for UiO-66/SB 200+EE sample

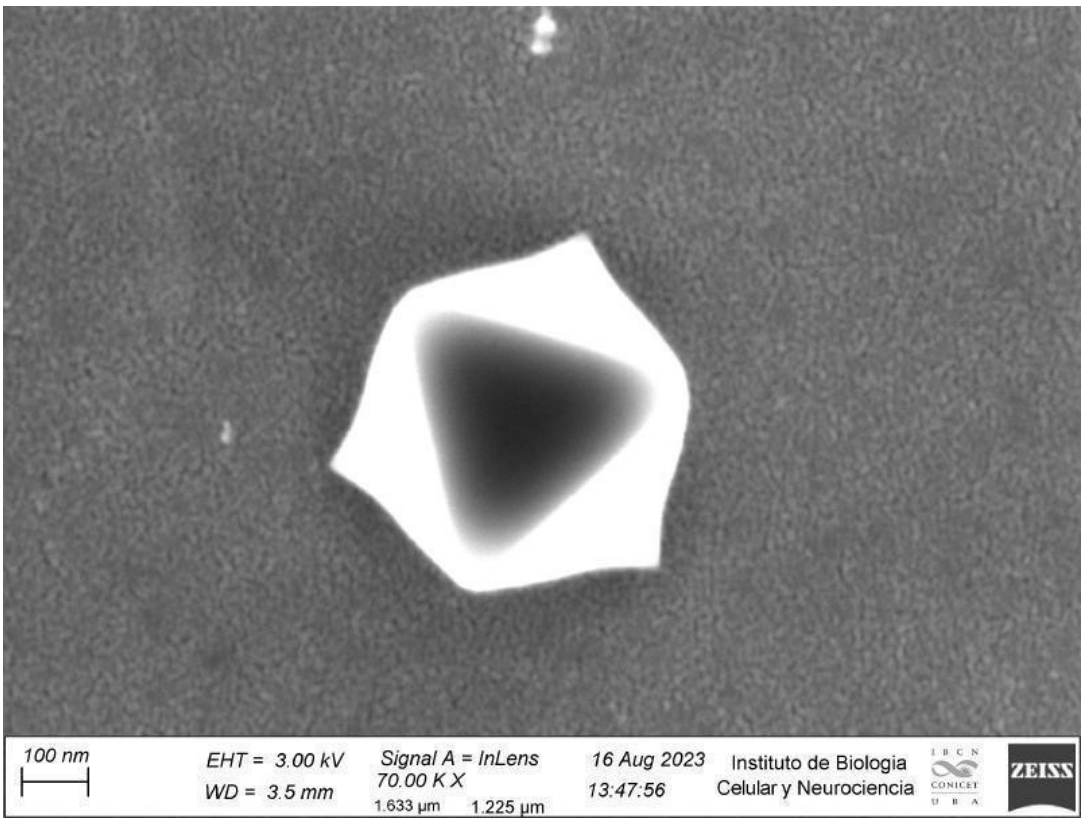

FIGURE S14. SEM for TB 350/UiO-66 sample

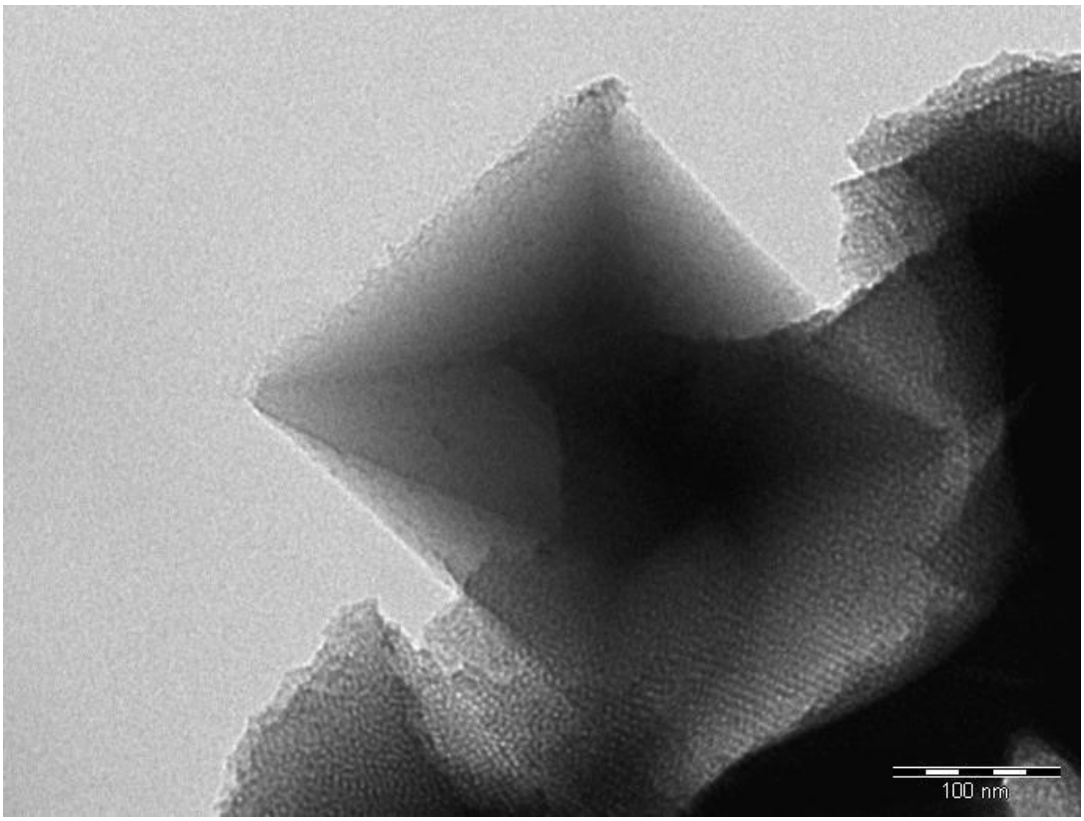

FIGURE S15. TEM for UiO-66/TB 200+EE sample

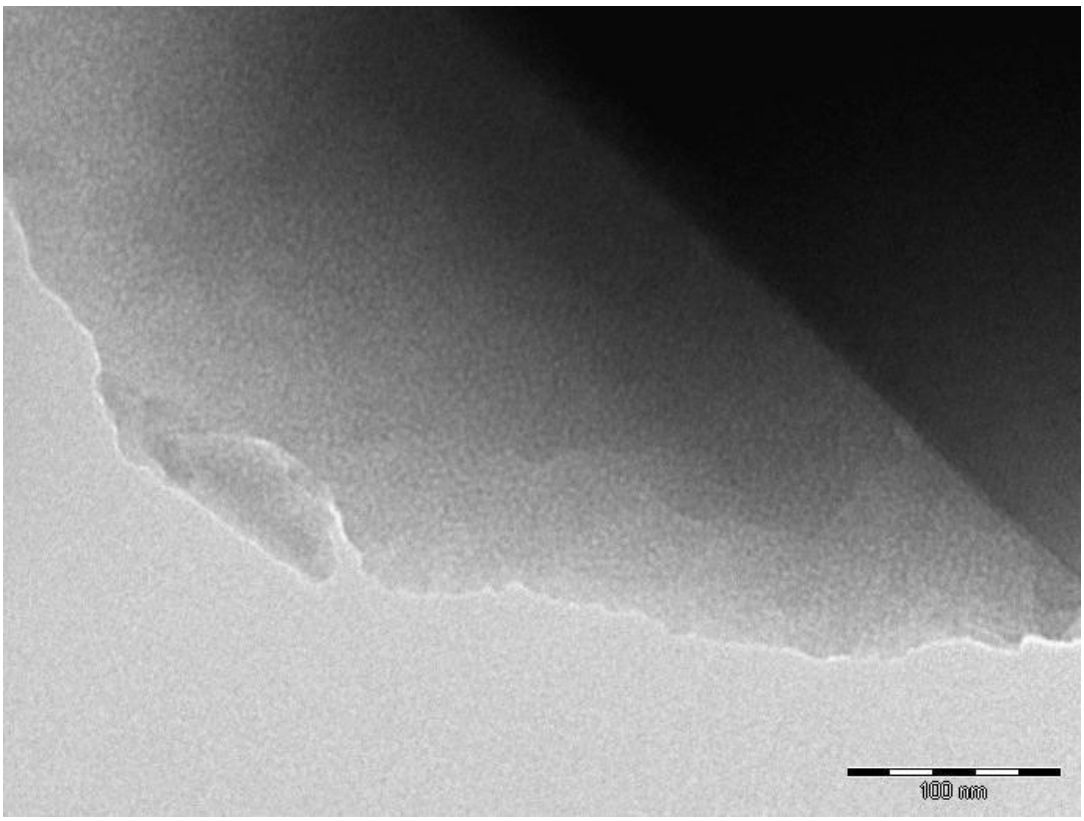

FIGURE S16. TEM for UiO-66/SB 200+EE sample

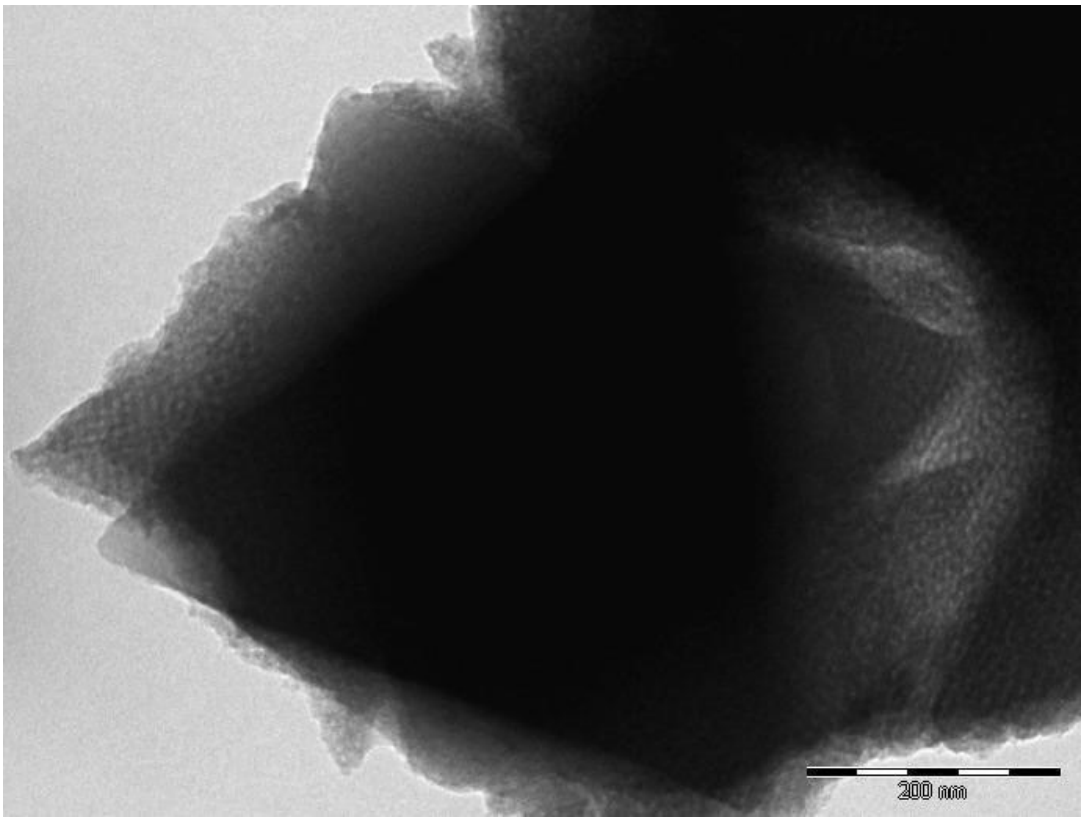

FIGURE S17. TEM for UiO-66/TF 200+EE sample

9. XRR experiments for UiO-66 and TB 200+EE bilayers

XRR measured at low and high humidity on different TB / UiO-66 bilayers.

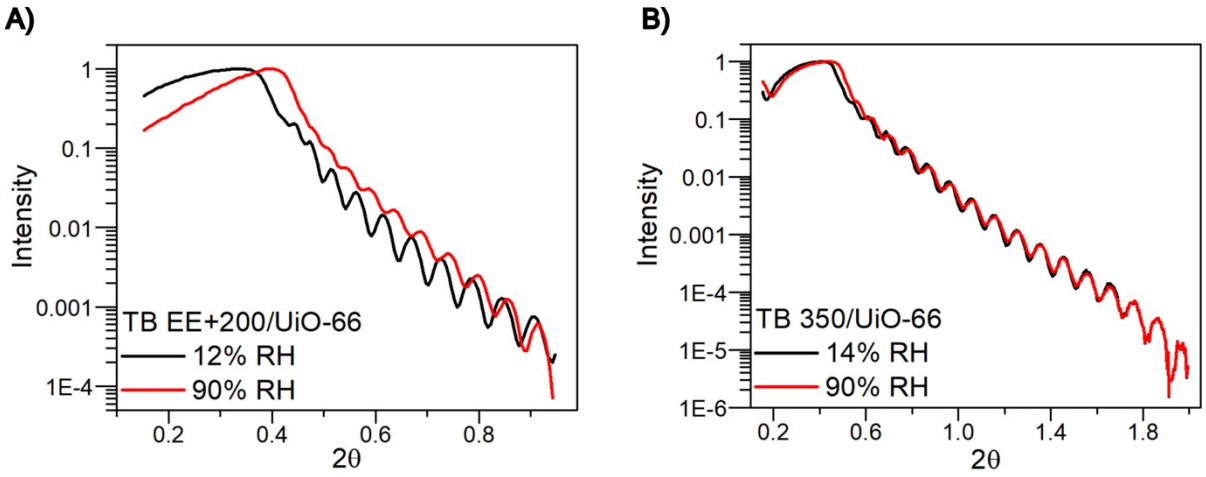

FIGURE S18. XRR experiments showing critical angle shift between low and high relative humidity conditions enabled by pore accessibility of bilayers to water.

10. **XRD of bilayers: peaks arising from UiO-66-LPE MOF crystalline structure and from mesoporous ordered structure.**

Grazing incidence (GI) XRD measurements were performed on bilayers prepared with MOFs and mesoporous layers. For each film, the presence of characteristic low angle diffraction peaks of UiO-66 was detected. Due to the relatively high intensity of (111) peak at approximately 2θ = 7.4 versus the (002) peak at approximately 2θ = 8.6, the (002) peak was not visible. It is also a valid hypothesis to assume some degree of preferential growth induced by the synthetic method employed.

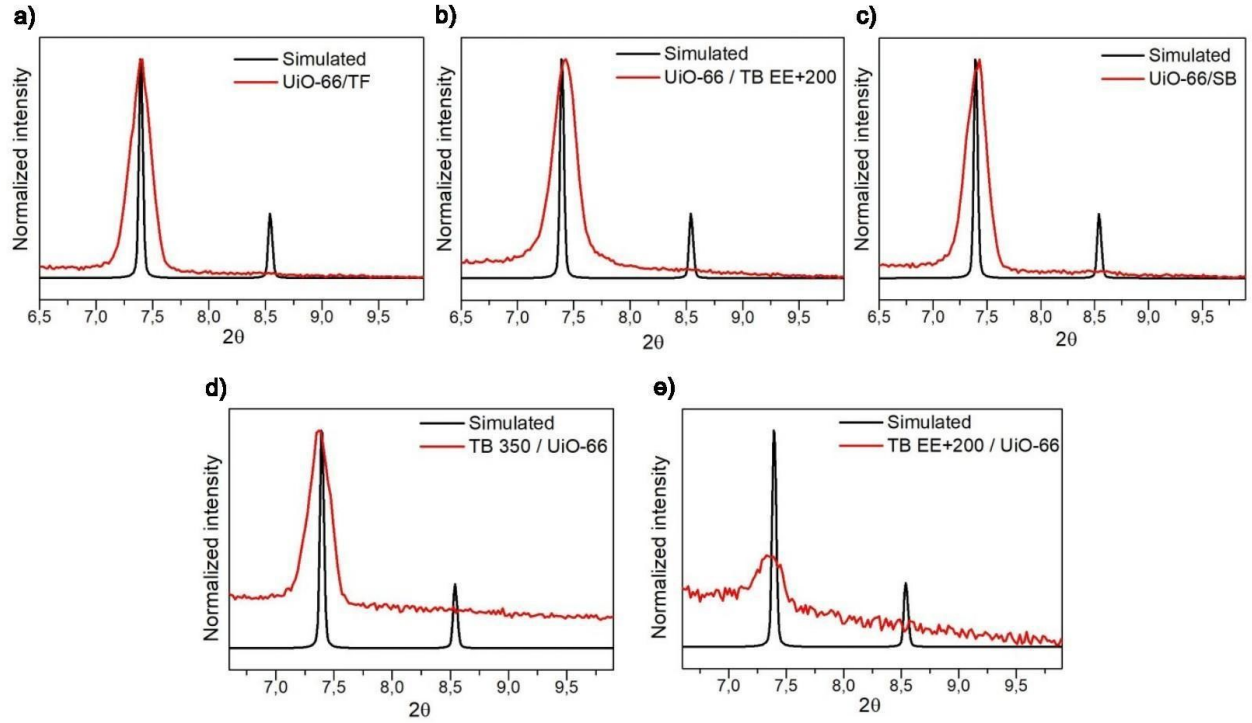

FIGURE S19. (a) GI-XRD pattern for UiO-66/TF 200+EE. **(b)** GI-XRD pattern for UiO-66/TB EE+200. **(c)** GI-XRD pattern for UiO-66/SB 200+EE. **(d)** GI-XRD pattern for TB 350/UiO-66. **(e)** GI-XRD pattern for TB EE+200/UiO-66.

11. XRR experiments for UiO-66/SB 200+EE bilayers

UiO-66/SB 200+EE films were characterized with XRR in high (90%) and low (8%) humidity with the critical angle position that shows the accessibility of pores.

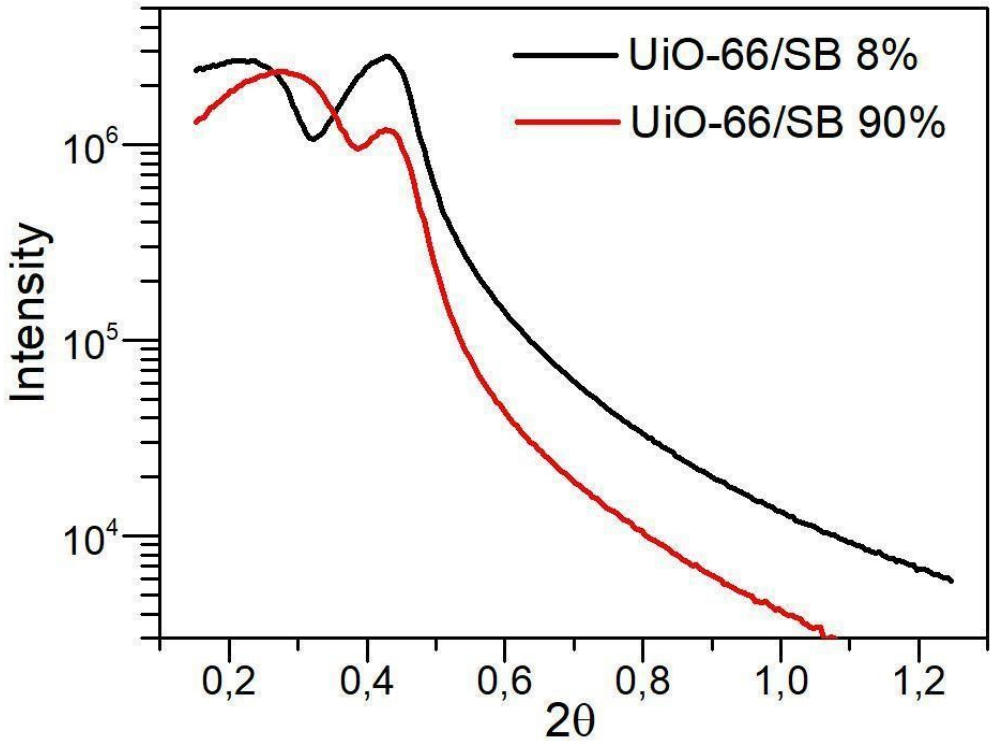

FIGURE S20. XRR experiments of UiO66/SB 200+EE sample, showing critical angle shift between low and high relative humidity conditions enabled by pore accessibility of bilayers to water.